IRSTI 31.15.15 https://doi.org/10.26577/IJBCh202619115

S. Gupta[1], A.P. Srivastava[2*], B.K. Pandey[3]

[1]Department of Chemistry, Poornima University, Jaipur (Rajasthan), India
[2]Department of Physics, Sanskriti University, Mathura, (UP), India
[3]Department of Physics and Material Science, Madan Mohan Malaviya University of Technology, Gorakhpur (UP), India
*e-mail: abhay.srivastava831@gmail.com

LANTHANUM-INDUCED ELECTRONIC TRANSITION IN HYDRIDE PEROVSKITES: A FIRST-PRINCIPLES STUDY OF $CsXH_3$ (X = Sc, Y, La, Ac)

Abstract: We studied the structural, mechanical, thermal, and electronic properties of cubic hydride perovskites $CsXH_3$ (X = Sc, Y, La, Ac) using first-principles DFT within the GGA-PBE and PAW schemes. The structural optimization and stability were studied using the third-order Birch-Murnaghan equation of state, and trends in the lattice parameters, bulk modulus, and compressibility were observed. The elastic constants and Voigt-Reuss-Hill approximations indicate mechanical stability. The phonon analysis shows no imaginary frequencies, which suggests dynamical stability. The thermal behavior is also characterized by a softening of the lattice with increasing cation size. Electronic structure results indicate metallic behavior of $CsScH_3$, $CsYH_3$, and $CsAcH_3$, while $CsLaH_3$ has a small band gap (~0.2 eV). Bonding shows that ionic character is present for $CsLaH_3$ with partial X–H covalency. This demonstrates the utility of cation engineering in hydride perovskites for hydrogen storage, conductive materials, and pressure-driven applications.

Keywords: Hydride perovskites, Density Functional Theory, Mechanical properties, Electronic structure, Cation engineering.

Introduction

The applications of hydrogen-rich materials are of great interest to materials scientists due to their high energy storage capacity, superconductivity, and efficient applications. In particular, metal hydrides and hydride perovskites have gained significant attention due to the combination of cheap, tunable electron-hydrogen with highly tunable form and mechanical properties (Chu et al., 2017; Zhang et al., 2023). Hydrogen in a crystalline lattice significantly influences a material's bonding and atomicity, indicating an interaction between ionic and covalent characteristics. Not only structural stability but also electronic transport, and therefore the electronic properties and lattice dynamics of these materials, are of particular importance, particularly for hydrogen storage technology (Almahmoud et al., 2025; Parvaiz et al., 2025).

Cubic perovskites with ABH_3 are a natural space for studying hydrides and provide a perfect platform: they have a very simple, stable structure. In these systems, the A cation and B cations electrostatically stabilize the lattice, and the B cation (X=Sc, Y, La, Ac) forms octahedral hydrogen coordination, giving rise to a three-dimensional network of corner-sharing XH_6 units (Kumar et al., 2026; Okumura 2024). The behavior of these materials is closely related to the B cation because of its ionic radius and electronic structure, and changes in these properties, which affect lattice expansion, bond strength, and orbital hybridization, have been reported in the literature in the last few years (Anaya et al., 2017; Kojima et al., 2009).

Previous theoretical work, such as that published in work of Masood et al. (2025), provides some useful insights into the architecture and mechanics of Cs-based hydrides. Yet there are some discrepancies in the elastic constants, the bulk modulus, and the thermal properties. This is because hydrides are highly sensitive to computational methods involving exchange-correlation functions, pseudopotentials, and convergence methods (Srivastava & Pandey, 2025b; Tanabe, 2009). Furthermore, while structural properties (e.g., structural constants or electronic properties) have had an initial look at, the lattice dynamics, bonding, and, in particular, electronic properties have been considered, but no complete and physical description of the dynamics of this family of cations was possible from both the physical and

© 2026 Al-Farabi Kazakh National University

theoretical perspectives on crystallization and cooling of solid cation profiles (Touati et al., 2024; Wang et al., 2022).

Fundamental physics is explained by hydride perovskites, which have the opposite: hydrogen acts as an anionic species at its sites, and transition-metal d orbitals have electrons near the hydride sites in the Fermi sea (Deng et al., 2025). The dual bonding gives rise to strong metallic conductivity, lattice softness, and strong electron-phonon coupling, which are very interesting for hydride applications, from conductive hydrides to potential superconductors, but with the full possibility of cation substitution (Benaissa et al., 2025).

In general, this paper presents the detailed first-principles calculations for cubic $CsXH_3$ (X = Sc, Y, La, Ac) hydrides. It provides a simple mechanical-electronic and mechanics-electronic discussion of their behavior. While research on heavy cations is well-established, this study is the first to show that cation-induced lattice expansion allows for a single physical interpretation of the material's elastic stiffness, phonon, and electronic properties (Chen et al., 2025; Gao et al., 2024). In particular, the combined analysis of phonon dispersion, density of states, and the electron localization function allows us to identify the origin of the dynamical stability and bonding behavior in cubic $CsLaH_3$ and to explain what occurs from the strongly metallic state to the near-semiconducting state in $CsLaH_3$ (Benaissa et al., 2025; Luo et al., 2023; Momma & Izumi, 2011; Tian et al., 2023). Moreover, we review all gaps in the previous literature about it to a certain extent and conclude that they were not due to the method, the chemistry, or the behavior of the hydride because, in view of the highly sensitive physical composition of the materials, we should take it with a big dose of salt and apply and make the predictions according to the specific methodology.

This study not only solidifies the notion of hydride perovskites but also promotes cation engineering as a suitable approach to tune mechanical robustness, thermal response, and electronic properties in hydrogen-rich materials, thereby advancing further research and development. Several theoretical reports have been published to date on Cs-based hydride perovskites, but the literature is fragmented and highly restricted to specific compounds such as $CsScH_3$ and $CsYH_3$, where elastic and thermal properties show very heterogeneous data.

In addition, there is an incomplete and inconsistent dataset for the full $CsXH_3$ (X = Sc, Y, La, Ac) series, particularly for $CsLaH_3$ and $CsAcH_3$. The contribution of the present work is to establish a comprehensive and standard first-principles analysis of this full series, covering structural, mechanical, phonon, thermal, and electronic properties within a single computational platform. Rather than following earlier work, we demonstrate a clear cation-driven tunability mechanism that links the size of the ion to lattice expansion, bonding strength, phonon softening, and the electronic transitions between the ions of interest. In addition, in $CsLaH_3$, we observed a metal-to-semiconductor transition and, with the aid of band structure, DOS, and ELF analysis, provided a new perspective on the role of cation substitution in hydride perovskites. This comprehensive design not only fills many gaps in the general literature, but also provides a physically consistent description of structure–property relationships, a prerequisite for the design of next-stage H-rich functional materials.

Computational methodology

Crystal Structure Initialization

The structure of the $CsXH_3$ (X = Sc, Y, La, Ac) was modeled using the ideal cubic perovskite structure with the space group $Pm\bar{3}m$ (No. 221). This is one of the simplest and most symmetric perovskite structures, and Cs atoms occupy the A-site position at the corners of the cube; in contrast, X atoms are in the B-site at the center of the body, and hydrogen atoms are in the face center (Waqas et al., 2021).

This allows for the formation of XH_6 octahedra from which every X atom is coupled to six hydrogen atoms. In these octahedra, their corner shares are made, and the lattice (in terms of orientation of atoms is also a unit of octahedra, so that these octahedra can be formed at either end of a three-dimensional lattice, i.e., XS = 0 from the start and S to the end. The Cs is present in the interstitial cavities created by these octahedra and stabilizes the lattice through electrostatic interaction between Cs and X atoms (Romero et al., 2024).

Cubic symmetry ensures that all X–H bond lengths and H–X–H bond angles are equal. This means physical properties are isotropic. This simplifies computations and the interpretation of the result. However, in a non-distorted structure, the fundamental material properties can be analyzed at the first step of the material structure without breaking symmetry (Srivastava et al., 2025b).

The structure can influence bonding, hybridization, and lattice behavior in many different ways. To begin with, the size of the X cation changes the lattice parameter and, therefore, the volume in such a way that they interfere with interatomic interactions more or less significantly. This makes

the chosen structure an ideal platform for studying the effects of cation substitution on physical properties (Belay et al., 2026).

Density Functional Theory Framework

All calculations were conducted using Density Functional Theory (DFT), which provides a quantum-mechanical description of the ground-state properties of many-electron systems. In this paper, the exchange-correlation interaction was analyzed using the generalized gradient approximation (GGA) within the PBE (Perdew-Burke-Ernzerhof) formulation. This function has been widely used for many years and simultaneously provides excellent functional analysis of the structural and electronic properties of electronic systems (Perdew et al., 1996).

The interaction between valence electrons and ionic cores was discussed by the Projector Augmented Wave (PAW) method. It reconstructs the all-electron wavefunction from the pseudo-wavefunction. It excels particularly for cases involving heavy and light atoms (La, Ac) because it accurately captures the electron density near the atomic cores (Blöchl, 1994).

We extended the electronic wavefunctions using a plane-wave basis set. The plane wave basis set is a desirable approach because its convergence is systematic, and periodic boundary conditions are more appropriate for an electronic system. Such periodic boundary conditions can support the accurate modeling of crystalline solids by accounting for surface effects when applying electronic wavefunctions in periodic systems. SCF calculations were made iteratively until the total energy and charge density converged. The Kohn-Sham equations were solved with the electron density to update the potential. This was done until all calculations converged, ensuring that the result was the correct ground state (Blöchl et al., 2005).

Plane-Wave Cutoff Energy and Convergence Testing

The choice of the plane-wave cutoff energy is very important in DFT calculations. In this work, we found a cutoff energy of 500–600 eV. This value was chosen not arbitrarily, but by carefully testing convergence. The calculations were performed at lower cutoff energies, and the system's total energy was investigated. Increasing the cutoff energy was gradually realized until the change in the total energy was negligible (typically less than 1 meV per atom). As we could not further increase the cutoff energy, this result was not unexpected (Hasan & Majidi, 2020).

A higher cutoff energy also makes the wavefunction and its representation that much cheaper and more efficient. We have chosen the most efficient cutoff (both in terms of details and in terms of computer efficiency for calculation) thus far. Similarly, convergence will also be possible with k points. We measure the output energy in large Monkhorst-Pack grids at an increasing number of k points. It is based on converging, and the structural (and electronic) properties are not negatively affected numerically. These kinds of convergence tests are necessary to give consistent results with the experimental results and provide reliable and reproducible comparisons of the different and similar compounds with the same computational platform (Srivastava & Pandey, 2025a).

Equation of State (EOS)

These are determined from the equilibrium structural parameters of $CsXH_3$ (X = Sc, Y, La, and Ac) using the energy–volume equation of state. To obtain total energy estimates for different unit cell volumes, compression and expansion were applied to the structure over the best volume range to fit the energy–volume relationship within ±5–10 percent of equilibrium space. From our analysis, we fit the energy–volume data for compression solids to the third-order Birch–Murnaghan equation of state, which is quite good at describing finite-strain behavior (Srivastava et al., 2024; Srivastava et al., 2025a).

The Birch–Murnaghan equation is expressed as (Srivastava et al., 2024; Srivastava et al., 2025a):

$$E(V) = E_0 + \frac{9B_0V_0}{16}\left\{\left[\left(\upsilon\right)^{-2/3} - 1\right]^3 K_0^{'} + \left[\left(\upsilon\right)^{-2/3} - 1\right]^2 \left[6 - 4\left(\upsilon\right)^{-2/3}\right]\right\} \quad (1)$$

where $\upsilon = \frac{V}{V_0}$.

From that fit, we extracted a few parameters. These are the equilibrium volume V_0, ground state energy E_0, bulk modulus (B_0), and pressure derivative (B_0'). Bulk modulus is the resistance of a material to the compression of volume. A higher value of B_0 indicates a stiffer lattice and more interactions between atoms, whereas a lower value implies the lattice is compressible. The pressure derivative B_0' refers to the difference in bulk modulus at a pressure level and, therefore, to anharmonic behavior of the lattice.

The curvature of the energy–volume curve near the equilibrium point is closely related to the bulk modulus. A sharper curve indicates a stiffer material, whereas a smaller one indicates a softer one. A Birch–Murnaghan fit is needed to provide a reliable, physically meaningful description of the compressibility behavior of such materials. This method provides a well-investigated framework for assessing structural stability, which can be directly evaluated through experimental and theoretical studies in the literature. It offers a strong basis for comparison with the data (Srivastava et al., 2025c).

Elastic and Mechanical Properties

The elastic properties were calculated using the stress-strain method, i.e., very light deformations to lower the optimized structure and to judge the stress response. The small strains, typically ±1 and 2%, were taken to various directions, and we obtained the stress tensors in a crystallographic way. For cubic systems, only three elastic constants (C_{11}, C_{12}, and C_{44}) need to be used; the failure resistance for the axial compression, volume change, and shear deformation are, respectively, of interest here (Guesmi et al., 2024).

The mechanical stability of the compounds was verified using the Born stability criteria (Guesmi et al., 2024):

$$\left\{\begin{array}{l} C_{11} > 0 \\ C_{44} > 0 \\ C_{11} - C_{12} > 0 \\ C_{11} + 2C_{12} > 0 \end{array}\right\} \quad (2)$$

Macroscopic mechanical properties were derived using the Voigt–Reuss–Hill averaging scheme. The Young's modulus (E) and Poisson's ratio (ν) were calculated using (Srivastava et al., 2025b):

$$E = \frac{9BG}{3B+G} \quad (3)$$

$$\nu = \frac{3B-2G}{2(3B+G)} \quad (4)$$

These parameters provide insight into stiffness, ductility, and bonding nature. Higher Young's modulus indicates a stiffer material, while Poisson's ratio reflects the degree of lateral deformation.

Phonon and Thermal Properties

The phonon properties were constructed using a supercell setup following the finite displacement method. We have been considering long-range processes and constructed a 2×2×2 supercell of small atomic displacement (~0.01 Å) and calculated the dynamical matrix forces. The phonon frequencies were determined by diagonalizing this matrix. The absence of imaginary frequencies indicates that the structure is dynamically stable. Thermal properties were then determined based on phonon and elastic data. The sound velocities were calculated, and the Debye temperature was determined by the equation (Srivastava & Pandey, 2025c; Srivastava et al., 2025b):

$$\theta_d = \frac{2\pi\hbar}{k_B}\left(\frac{3n}{4\pi V}\right)^{1/3} v_m \quad (5)$$

The Debye temperature is related to lattice vibrations and provides insight into thermal conductivity and heat capacity. Higher values indicate stronger bonding and higher vibrational frequencies.

2.7 Electronic Structure and ELF Analysis:

The electronic structure was investigated as a function of the band structure and density of states. The band structure was computed as a function of the high-symmetry branches in the Brillouin zone. Also, the total and partial density of states were determined to capture the effect of the different atomic orbitals. For this purpose, the Fermi level was set at 0 eV. To determine whether the material is metallic or semiconducting, the band gap was measured (Srivastava et al., 2025b).

We have also calculated the electron localization function (ELF) to understand chemical bonding. The

ELF ranges from 0 to 1, where values close to 1 indicate strong electron localization and values close to 0 indicate delocalized electrons. The ELF analysis is a good way of getting a real-time understanding of bonding. It also allows for distinguishing between ionic and covalent interactions, but also provides an unbiased way to understand the electronic and structural dynamics of covalent interactions (Srivastava & Pandey, 2025c).

Electronic band structures were computed along the high-symmetry path Γ→X→M→Γ→R→X→M→R in the Brillouin zone. The band gap was determined as (Srivastava & Pandey, 2025c; Srivastava et al., 2025b):

$$E_g = E_{CBM} - E_{VBM} \quad (6)$$

The total density of states was calculated as:

$$D(E) = \delta(E - E_{nk}) \quad (7)$$

and orbital-projected DOS was obtained for Mn-3d, Bi-6p, and Te-5p states.

Electron localization was analyzed using the Electron Localization Function (ELF), defined as (Srivastava & Pandey, 2025c; Srivastava et al., 2025b):

$$ELF = \left[1 + \frac{D}{D_h}\right]^{-2} \quad (8)$$

Results and discussion

Structural Properties

Crystal Structure

Figure 1 shows the crystal structure of the cubic $CsXH_3$ (X = Sc, Y, La, Ac) cubic lattice that belongs to the family of perovskite. The Cs^+ ions are located at the cube corners, the X^{3+} ions are at the center of the body, and the H^- ions are in the faces. Together, they form a very symmetrical cubic crystallographic lattice with space group $Pm\bar{3}m$ (No. 221). In such a case, all the directions follow one another, and its structure and physical properties are the same.

The central X^{3+} cation is surrounded by six H^- ions and the octahedral coordination geometry of this coordination field (XH_6). This means that the coordination of X is 6 and therefore that the octahedra are the basic unit of structure of the crystal. 12 H ions coordinate the Cs^+ ions, and hence, in this Cs^+ cation, it creates a cuboctahedral area, as is frequently the case with A-site cations in perovskites. The H^- ions also interact with neighboring X^{3+} cations, forming a continuous 3D structure of corner-connected octahedra.

Figure 1

Crystal structure of cubic $CsXH_3$ (X = Sc, Y, La, Ac) with $Pm\bar{3}m$ symmetry, showing Cs^+ at cube corners, X^{3+} at the body center, and H^- at face centers, forming octahedral XH_6 units and a 3D perovskite framework

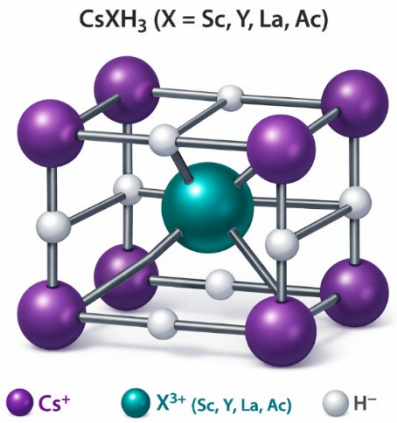

From a physical standpoint, the structure is kept stable by the strong electrostatic interaction between Cs^+, X^{3+} ions, and H^- ions, and hence the overall charge concentration is neutral. The X–H bonding is where the X^{3+} ion becomes very attractive and attracts all the hydride ions to form a tight stable octahedral structure. And, to some extent, the Cs^+ ion remains in the position it must occupy, helping to stabilize the structure and influencing the lattice parameters.

All X–H bond lengths and bond angles are equal, and the cubic symmetry in Figure denotes a perfect and undistorted phase. The high symmetry of this configuration is significant because it creates isotropic mechanical, electronic, and thermal properties. The size of the X cation (from Sc to Ac) might alter the lattice constant, bonding strength, and stability of the X cation, or change its structure in response to pressure and temperature.

Essentially, this is a typical hydride perovskite structure where it consists of corner-sharing XH_6 octahedra, which together make up a strong 3D frame (see Fig. 1). Cs^+ ions in that network can be easily incorporated. The various octahedra at the site differ significantly at different levels, and their electronic, bonding, and pressure-response properties vary

across that network. As a result, it finds applications in fields such as energy storage, hydrogen generation, and many other high-value technologies.

Energy-Volume Curve

The curve shown in Fig. 2 (a-d) is the energy-volume (E-V) curve of cubic $CsXH_3$ (X = Sc, Y, La, Ac) fitted in DFT with the Murnaghan equation of state (EOS). Each curve is a smooth parabolic shape, a clear indication of a stable crystalline phase. The minimum point of each curve (black dot) represents the equilibrium volume and ground-state energy in the figure. This is the case when no external gravitational forces are acting on the system.

Figure 2

Energy–volume curves of cubic $CsXH_3$ (X = Sc, Y, La, Ac) showing DFT results and Birch–Murnaghan fits, indicating equilibrium volume, mechanical stability, and compressibility trends across the series

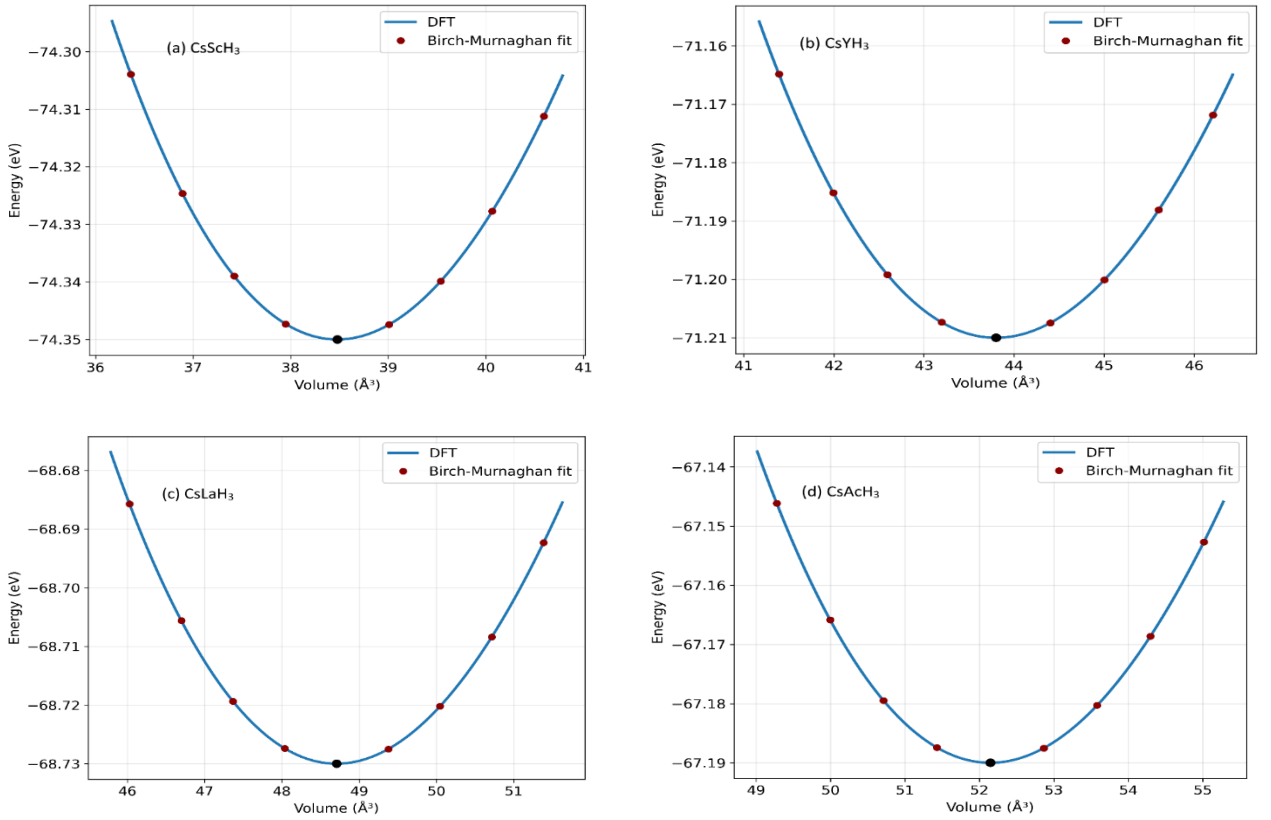

From a physics point of view, the curvature of the E–V curve appears to relate to the bulk modulus B_0, which measures how hard the material is to compress. The thicker curve with a larger parabola means better bulk modulus, stiffness, and less compressibility. A flatter curve means a softer lattice structure. The curvature of $CsScH_3$ with bond size and stiffness is stronger compared to the curvature of $CsAcH_3$, which makes it easier to compress the material because of the larger ionic size and the weaker bonding.

The equilibrium volume shifts from $CsScH_3 \rightarrow CsYH_3 \rightarrow CsLaH_3 \rightarrow CsAcH_3$ due to the increase in ionic radius of the X^{3+} cation. As cations grow larger, the unit cell volume must increase (since the lattice does not overlap with the atoms like X–H), and the bonding weakens. This means that the cohesive energy becomes less negative, which, in turn, can increase the binding strength across our range of compounds.

The excellent agreement between the DFT data (blue line) and the Birch–Murnaghan fit (red points) validates the EOS fit and confirms that we can apply standard compressibility behavior to volume changes. This method can extract relevant thermodynamic parameters, such as the equilibrium

volume, bulk modulus, and its pressure derivative, which are important for understanding the dynamics of volume changes under pressure.

From a stability perspective, a single minimum in each curve indicates that all the compounds are thermodynamically stable in the cubic phase at zero pressure. There are no small missing minima or irregularities; none of the competing phases are energetically favorable in this volume range. The smoothness of the curves suggests good convergence of DFT calculations (at least numerically) at this moment in time with a given mean parameter.

In general, the figure shows that structural stability, bonding strength, and compressibility evolve systematically with the choice of X cation, largely due to ionic size effects and changes in the X–H interaction strength. These trends play a key role in predicting material behavior under pressure and in the design of hydride-based functional materials.

Structural Parameters optimized by DFT

In summary, Table 1 shows equilibrium structural and elastic properties of $CsXH_3$ (X = Sc, Y, La, Ac) from DFT as shown at Table 1. A clear trend appears from the lattice constant (a) and equilibrium volume in the equilibrium form (V_0) that is determined from Sc → Y → La → Ac. This is due to the increasing ionic radius of the X^{3+} cation, which widens the lattice spacing and brings the ions closer together. It has a large tendency to be more favorable for ground state energy (E_0) if we see it is less than (−74.35 → −67.19 eV (i.e., larger) and increase the coupling strength from X–H orbital overlap at the poles is reduced. The E_0 decreases the strength of the whole system, as the electrostatic interaction decreases for all.

The bulk modulus decreases drastically from 116.18 GPa ($CsScH_3$) to 82.03 GPa ($CsAcH_3$), which indicates a softer and more compact material in the case of growth of cations. Smaller, more compact structures, for instance, should be more compressed because of stronger interactions among the atoms, but larger lattices are stronger in terms of restoring forces. Surprisingly, the pressure derivative B_0' remains very close to 3.4-3.7 in all cases, and the response and mechanical stability of all compounds under compression are well maintained.

Table 1

Calculated equilibrium structural and mechanical parameters via DFT of cubic $CsXH_3$ (X = Sc, Y, La, Ac), including lattice constant (a), equilibrium volume (V_0), ground-state energy (E_0), bulk modulus (B), and its pressure derivative (B'), with comparison to reported values from reference (Masood et al., 2025)

Compound	a (Å)	V_0 (Å³)	E_0 (eV)	B (GPa)	B'
$CsScH_3$	3.376	38.478	-74.35	116.18	3.700
	3.466*	41.637*	-25.112*	130.82*	3.999*
$CsYH_3$	3.525	43.8	-71.21	100.14	3.600
	3.655*	48.827	-25.254*	119*	3.987*
$CsLaH_3$	3.652	48.707	-68.73	88.68	3.400
$CsAcH_3$	3.736	52.146	-67.19	82.03	3.400

**(Masood et al., 2025)*

Compared with reference (Masood et al., 2025), the results for a and V_0 are large. In particular, $CsScH_3$ is at 3.466 Å and B_0 = 130.82 GPa from this work, with a = 3.376 Å and B = 116.18 GPa in. Another reason the E_0 values of $CsYH_3$ differ is that they are in fact (e.g., −74.35 eV vs −25.112 eV), which is not necessarily physically relevant. The reason is that A and B_0 correspond to different energy reference schemes: the total energy is normalized between cells, the energy is pseudopotential, and the core electrons are included or excluded. Thus, we should compare only relative trends in E_0 within the same calculation perspective.

The reasons for the variances from work of Masood et al. (2025), are not surprising. First off, different studies tend to use different exchange–correlation functionals (e.g., GGA-PBE), which are directly related to lattice size and bonding strength. The second is variations in pseudopotentials (PAW vs. norm-conserving), which can also affect total energy and equilibrium values. Thirdly, the range of the equation-of-state fit and the data density also

affect the values of B_0 and B_0'. The fact that the DFT is performed at zero temperature can affect the value in fact – in some publications, temperature is only at least implicitly a factor, leading to a slightly higher lattice value for the former equation.

From an application and process standpoint, it is really useful to know what work has been done in these applications. With the largest bulk modulus and the most negative E_0, $CsScH_3$ is the most mechanically stable and rigid. This is a very suitable material for pressure-resistant and structural applications. $CsLaH_3$, with larger volumes and lower bulk moduli, makes hydrogen compressible. The various components that help operate the X-site cation can guide the development of functional hydride materials, energy storage systems, and pressure-dependent devices.

Mechanical Properties

Elastic Constants

In Table 2 we report the independent elastic constants for cubic $CsXH_3$ (X = Sc, Y, La, Ac), namely C_{11}, C_{12}, and C_{44}, which characterize the crystal's response towards different forms of mechanical deformation. In a cubic system, C_{11} measures the mechanical resistance against longitudinal compression along their main vertical and lateral directions, and C_{12} corresponds to strain along one axis/stress, and C_{44} is related to shear deformation at the same time. The independent elastic constants are very important as they indicate mechanical stability with rigidity, and we are concerned with the properties of the material.

Table 2

Calculated single-crystal elastic constants C_{11}, C_{12}, and C_{44} of cubic $CsXH_3$ (X = Sc, Y, La, Ac), compared with available literature values from reference (Masood et al., 2025)

Compound	C_{11} (GPa)	C_{12} (GPa)	C_{44} (GPa)
$CsScH_3$	209.12	69.71	69.71
	350.68*	78.71*	84.06*
$CsYH_3$	180.25	60.08	60.08
	448.75*	62.49*	99.55*
$CsLaH_3$	159.62	53.21	53.21
$CsAcH_3$	147.65	49.22	49.22

**(Masood et al., 2025)*

The data show a sharp trend in both elastic constants: the elastic constants of $CsScH_3$ decrease from 209.12 GPa to 147.65 GPa in $CsAcH_3$, and C_{44} decreases from 69.71 GPa to 49.22 GPa as well. For example, the structural data show that when an X-site cation is shifted from Sc to Ac, not only does the lattice length increase, but the bond lengths also increase. The result is that the lattice becomes less rigid and easier to deform because the ions are larger; at the same time, the material interaction between X and H is stronger. With a larger atomic structure, the restoring force against compression and shear is weakened. So $CsScH_3$ is the stiffest part of the series, whilst $CsAcH_3$ is the softest.

These values also further support the mechanical stability of the cubic phase. The Born stability conditions for a cubic crystal are $C_{11} > 0$, $C_{44} > 0$, $C_{11} - C_{12} > 0$, and $C_{11} + 2C_{12} > 0$. The mentioned values satisfy these conditions for each compound. For example, in $CsScH_3$, $C_{11} - C_{12}$ = 139.41 GPa (positive), and the same holds in the case of other compounds. This means that all four hydrides remain mechanically stable in the cubic phase and do not undergo structural collapse under pressure or shear stress.

Although C_{11} is a much bigger number than C_{12} and C_{44} for all compounds, this shows that the crystal resists direct axial compression more strongly than shear distortion. That is, it is harder to squeeze the lattice along a crystal axis than to distort it sideways. In most ionic and partially covalent systems, a lot of the bonding network is responsible for the bond length change, so the structure is more easily disrupted due to a strong X–H interaction. In hydride perovskites, the structure is strongly influenced by the octahedral arrangement of atoms, as evidenced by the observed elasticity.

As compared to literature reference (Masood et al., 2025), the absolute values of C_{11} and C_{44} reported are much higher than those of the present study, especially for $CsScH_3$ and $CsYH_3$. For example, for $CsScH_3$, it was reported that C_{11} = 350.68 GPa, but the present value is 209.12 GPa. As for $CsYH_3$, it was given in work of Masood et al. (2025), with C_{11} = 448.75 GPa, and our current value is 180.25 GPa. The deviation is larger for C_{11} and C_{44}. Consequently, this paper implies much stiffer lattices, especially against axial compression and shear.

Now we can explore how we can explain this deviation in physically reasonable ways. We find that the elastic constants are very sensitive to the equilibrium lattice parameter, the exchange-correlation functional, and the method used to compute the stress-strain response. A calculation like

ours will lead to a smaller equilibrium structure for the different atoms, and therefore stronger bonding between them, which will naturally give higher values for C_{11} and C_{44}. Likewise, the difference in pseudopotentials, cutoff energy, k-point mesh, strain amplitude, fitting procedure, and convergence threshold may lead to a severe impact on the second derivative of the total energy from which we obtain elastic constants. This means that deviations are usually larger for elastic constants than for lattice constants.

There's also a deeper physical reason why the literature's values may differ. Hydride systems contain very light hydrogen atoms, and the bonding environment is particularly sensitive to the electronic charge distribution and local strain relaxation. If one of our analyses allows for more complete internal relaxation under strain while the other method uses a different approximation, then the shear and axial stiffness can be drastically altered. Because the differences do not mean that one dataset is wrong, we would say it is a telling signal that the elastic properties are very method-dependent in hydrogen-rich solids, and the bulk of these data is relatively consistent, with smaller-cation compounds being much stiffer than larger-cation ones.

The available elastic constants are therefore very useful in the applications: $CsScH_3$ is most suitable for mechanical rigidity, stress resistance, and structural durability under pressure. This material becomes good for pressure-tolerant hydride systems and for mechanically stable solid-state products, whereas $CsLaH_3$ and $CsAcH_3$ seem softer at the macro level. They can deform at a lesser weight, which is useful for hydrogen systems, which are characterized by a tighter lattice that enables more hydrogen movement and less strain and energy at work. As a result, basic mechanical behavior is closely linked to material selection through elastic data.

Finally, in Table 2, we also see that the elastic response of $CsXH_3$ is strongly dependent on the size of the X-site cation and the strength of the X–H bonding network. Our results show that the cubic phases are mechanically stable for all compounds and that there is a systematic softening from Sc to Ac. A couple of important differences are seen in our results compared to those in work of Masood et al. (2025), but one cannot stop the physical progression due to the bonding change. The physical phenomenon is also not surprising as we consider the lattice expansion for an atomic solution, but it is taken into account with the theoretical approach.

Elastic Modulus

Table 3 shows the calculated elastic properties–bulk modulus (B), shear modulus (G), Young's modulus (E), and Poisson's ratio (ν)–of cubic $CsXH_3$ compounds (X = Sc, Y, La, Ac) and the literature values available from work of Masood et al. (2025), for $CsScH_3$ and $CsYH_3$. All elastic moduli decrease clearly with the cation change from Sc to Ac. In particular, the bulk modulus drops from 116.18 GPa for $CsScH_3$ to 82.03 GPa for $CsAcH_3$, the shear modulus from 69.71 GPa to 49.22 GPa, and Young's modulus in a way that is progressive from 174.27 GPa to 123.04 GPa.

Table 3

Calculated bulk modulus (B), shear modulus (G), Young's modulus (E), and Poisson's ratio (ν) of cubic $CsXH_3$ (X = Sc, Y, La, Ac), with comparison to literature values from reference (Masood et al., 2025)

Compound	B (GPa)	G (GPa)	E (GPa)	ν
$CsScH_3$	116.18	69.71	174.27	0.26
	130.82*	100.55*	252.68*	0.27*
$CsYH_3$	100.14	60.08	150.21	0.26
	119*	107.33*	276.23*	0.29*
$CsLaH_3$	88.68	53.21	133.02	0.24
$CsAcH_3$	82.03	49.22	123.04	0.23

**(Masood et al., 2025)*

This means that the materials are becoming softer, more compressible, and less resistant to shear and tensile deformation over the course of the series. The main reason for this is the increase in ionic radius of the X^{3+} cation (Sc → Y → La → Ac), which results in lattice expansion and an increase in interatomic separation, which weakens X–H bonding strength. As a result, the resistance to volume compression and shear deformation decreases, thereby reducing the material's overall stiffness.

Compared with literature values, the results for $CsScH_3$ and $CsYH_3$ are lower, but the trend remains in good agreement. As an example, the bulk modulus of $CsScH_3$ is 116.18 GPa in this study compared to 130.82 GPa found in work of Masood et al., 2025, while for $CsYH_3$ it is 100.14 GPa in this study compared to 119 GPa found in work of Masood et al. (2025). Similarly, the shear modulus and Young's modulus differ significantly, with higher values reported in work of Masood et al. (2025). These differences can be attributed to different methods

used to compute these values, such as the exchange–correlation functional, pseudopotentials, and convergence parameters, as well as to the limitations of standard DFT for particle interactions.

The Poisson's ratio is slightly lower, from 0.26 to 0.23 across the entire series, suggesting a gradual decrease in ductility and a more directional bonding. From a practical point of view, compounds like $CsScH_3$ and $CsYH_3$, which have higher elastic moduli, are more suitable for mechanically strong and high-pressure environments, while $CsLaH_3$ and $CsAcH_3$, with lower stiffness, may be advantageous for compressibility and structural flexibility. In general, the results show that cation size, bonding strength, and mechanical properties are well-related in Cs-based hydride perovskites.

Thermal Properties

Phonon Dispersion Curve

Figure 3 (a–d) is the phonon dispersion curves of cubic $CsXH_3$ (X = Sc, Y, La, Ac) along high-symmetry directions (Γ–X–M–Γ–R–X–M–R) in the Brillouin zone. These are phonons that propagate through the crystal, moving outward, and play a very useful role in the dynamics of crystal molecules. The main observation of this region is that all those phonon frequencies are positive in the Brillouin zone for every compound. There are no imaginary (negative) frequencies in this region, and that is precisely the assurance that, in this cubic area, all structures are dynamically stable. To put it another way, the lattice will not move up or down for small atomic displacements and does not suddenly distort.

Figure 3

Phonon dispersion curves of cubic $CsXH_3$ (X = Sc, Y, La, Ac) showing absence of imaginary frequencies, confirming dynamical stability and revealing systematic phonon softening with increasing cation size

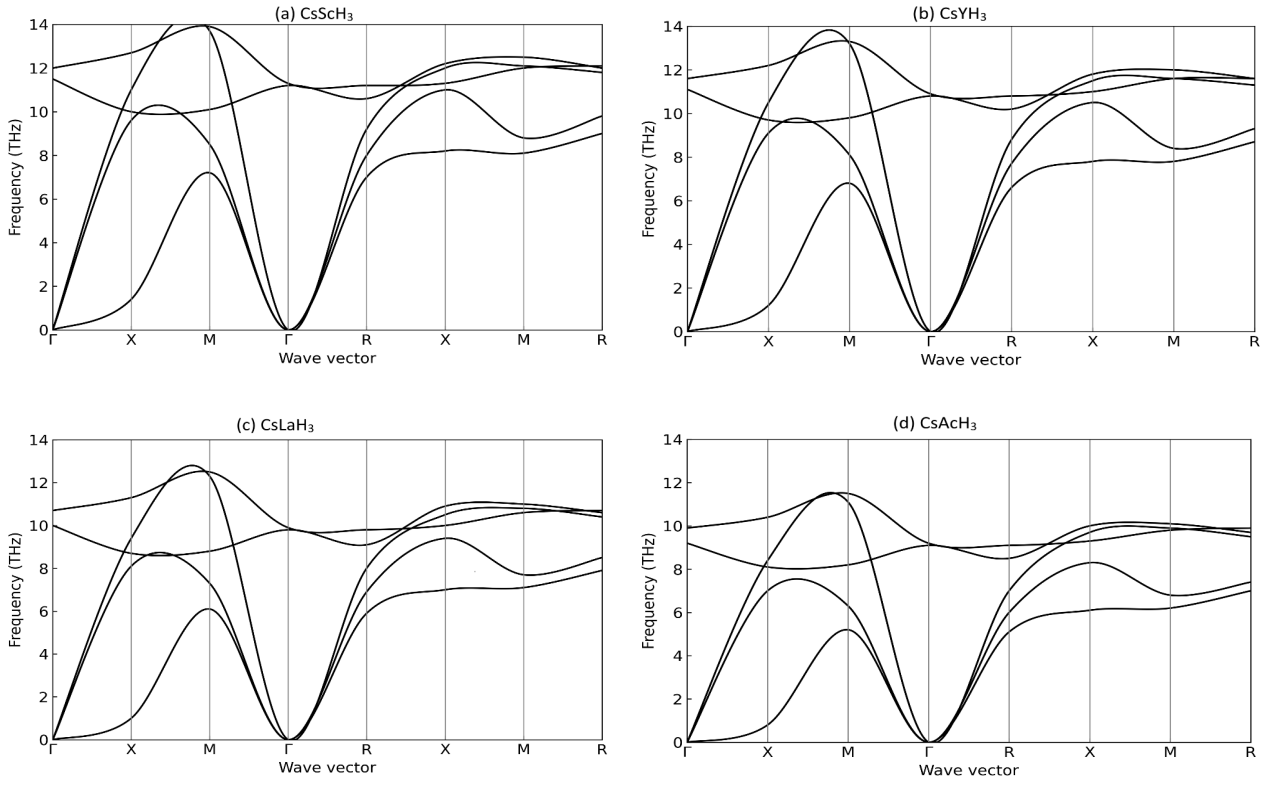

Every phonon spectrum has different acoustic and optical branches. Since the three acoustic modes start at zero frequency at the Γ-point and are collective vibrations (long-wavelength sound waves), the higher frequencies correspond to optical phonons, which primarily involve the motion of the lighter H^- ions relative to the heavier Cs^+/X^{3+} ions. Since hydrogen is very light, it plays a major role at high frequencies (the Γ-point) in the upper part of the spectrum (~10–14 THz). This is a common feature of metal hydrides.

From $CsScH_3$ to $CsAcH_3$, one can find very readily that the phonon frequencies are decreasing in the optical region. On $CsScH_3$, the maximum frequencies occur around 14 THz, and for $CsAcH_3$, lower values are observed (10-11 THz on the other hand). This process can also be explained via the main formula (Zhang et al., 2023) we use, where ω is the phonon frequency, k is the constant of the effective force, and m is the mass of the X cation. From Sc to Ac, there are two effects (the mass of the X cation increases and the X–H bond becomes weaker as the lattice expands).

Also, the phonon band does not reach negative regions close to high symmetry points (Γ, M, R). Imaginary modes are also prevalent in unstable perovskites and may also be used for structural instability (i.e., tilting in octahedral, phase changes). But the XH_6 octahedral framework survives, and there are no soft modes. This means the exact cubic structure is not just physically stable in one case but vibrationally stable as well without loss.

The dispersion (spread) of phonon branches also provides some bonding information. $CsScH_3$ has relatively wide dispersion, indicating stronger interatomic interactions and better phonon propagation. $CsLaH_3$ and $CsAcH_3$ both tend to have flatter branches, reflecting weaker interactions and more localized vibrations. This is consistent with elastic and EOS data, which show that stiffness decreases with increasing cation size.

In the thermodynamic sense, these materials have coherent phonon spectra that can predict strongly vibrational free energy, heat capacity, and entropy. The absence of imaginary modes gives very thermodynamic values on Debye temperature and thermal expansion to the materials, so that we could easily observe them. Moreover, our high-frequency hydrogen spectra indicate that these materials have high Debye temperatures, at least in $CsScH_3$, and this might mean they have easier structural stability and better conductivity.

For different applications, these results are very important. Dynamically stable hydrides like $CsXH_3$ should be considered for hydrogen storage, solid-state energy systems, and pressure-dependent functional materials for high-temperature and high-pressure applications. The higher frequencies of the phonons in $CsScH_3$ imply more robust bonding and temperature stability, and these materials are therefore ideal candidates for energy storage and transport in high-temperature as well as high-pressure situations. A less flexible structure is observed in the cases of $CsLaH_3$ and $CsAcH_3$; this can reduce the atomic lattice flexibility, which also reduces hydrogen diffusion and transport of ions.

Overall, Figure 3 confirms that all $CsXH_3$ compounds are dynamically stable cubic hydrides, with lattice dynamics strongly influenced by the mass and size of the X cation. The systematic softening of phonon modes from Sc to Ac can be clearly described in terms of structural expansion, weakened bonding, and reduced elastic stiffness, providing a complete and coherent physical picture of these materials.

Thermal Parameters optimized by DFT

Table 4 summarizes the acoustic properties and thermal response of $CsXH_3$ (X = Sc, Y, La, Ac) as well as the anisotropy factor (A), transverse (V_t), longitudinal (V_l), and average (V_m) sound velocities, together with the Debye temperature (θ_D). We see that they can also be calculated based directly on the elastic moduli and density, and reflect how elastic waves propagate and how this lattice stores the vibrational energy. So V_t, V_l, V_m, and θD decrease systematically from $CsScH_3$ to $CsAcH_3$ (Vm is from 3317.59 m/s ($CsScH_3$) to 2291.09 m/s ($CsAcH_3$), or from 500.29 K to 312.2 K). The lattice is softer and thus less connected with X cations as we go up in size of $CsAcH_3$.

We can easily learn why there is this trend. Sound velocity is proportional to √(elastic modulus/density). Increasing the density of X atoms increases the density of the sample and is clearly related to the reduction in elastic stiffness in the lattice by decreasing the B and G. Increasing the density leads to a loss of restoring force against the displacement of atoms and phonon velocities. Since the Debye temperature is related to the maximum frequency of the phonons, when the sound velocity is less than it is, its characteristic vibrational energy is lower, and its acoustic spectrum is smaller. It is consistent with the phonon dispersion results, such as the downward frequency shift from Sc to Ac.

Table 4
Calculated elastic anisotropy factor (A), transverse (V_t), longitudinal (V_l), and average (V_m) sound velocities, and Debye temperature (θ_D) of cubic $CsXH_3$ (X = Sc, Y, La, Ac), with comparison to literature values from reference (Masood et al., 2025)

Compound	A	V_t (m/s)	V_l(m/s)	V_m (m/s)	θ_D(K)
$CsScH_3$	1.2	2988.31	5175.86	3317.59	500.29
	0.34*	3765.881*	6641.094*	4187.289*	604.9*
$CsYH_3$	1.25	2654.74	4598.5	2947.44	425.68
	1.38*	3349.403*	6345.873*	3744.507*	541*
$CsLaH_3$	1.35	2383.67	4127.52	2645.63	368.81
$CsAcH_3$	1.45	2064.01	3574.39	2291.09	312.2

**(Masood et al., 2025)*

The anisotropy factor (A) increases from 1.2 to 1.45, which means that the material becomes slightly more elastically anisotropic as it grows in size. As $CsScH_3$ is more isotropic, a small deviation in $CsAcH_3$ indicates a direction-dependent elastic response. This may reflect better structural flexibility and weaker directional bonding in larger cation systems.

The sound velocities and Debye temperature have always been higher in the literature, while the other results are more favorable or not, for $CsScH_3$, to the value of 4187.289 m/s and θ_D = 604.9 K in the literature, while in our work, it is 3317.59 m/s and 500.29 K. The same for $CsYH_3$ in the literature also. These higher values in work of Masood et al. (2025), mean a stiffer material and stronger bonds in their calculation. However, the general trend is still the same for all compounds, so that both are really quite similar.

In fact, there are multiple reasons that may explain the differences. First, the sound velocities and the Debye temperature are highly sensitive to elastic constants and minor differences in C_{11}, C_{12} and C_{44} can potentially result in enormous changes in values for Vm and θ_D. Second, the correct choice of exchange-correlation functional, pseudopotential, and structural design can yield different elastic moduli and densities. Third, in addition to the vibrational properties of atoms and molecules, electronic structures that consist of hydrogen are very sensitive to the experimental results in this article. Finally, the value of the anisotropy factor (A) for $CsScH_3$ (0.34) is very different from the present value (1.2), and this may be due to the way the values can be estimated.

From a practical point of view, the results obtained could be extremely useful in any application. $CsScH_3$ (the one with the highest sound velocity and Debye temperature) has good interatomic bonding potential; high thermal conductivity, and better resistance to lattice vibrations, making it suitable for applications at high temperature or mechanically stable. $CsLaH_3$ and $CsAcH_3$ (low θ_D and sound velocity) have a milder phonon behavior, which could therefore be helpful in hydrogen diffusion, thermal insulation, and energy storage work for materials with lattice stiffness that can lead to motion by atoms in hydrogen.

In contrast, a lower Debye temperature implies higher phonon scattering from the molecule (e.g., soft noise) and lower thermal conductivity. Low Debye also implies that $CsLaH_3$ can be helpful for thermoelectric or thermal barrier materials in applications for building or systems for storage of energy supply, in which $CsLaH_3$ is used along with different materials, so that high Debye temperature is not only the dominant temperature parameter in the construction process, but also the least sound velocity.

Overall, Table 4 clearly shows that lattice dynamics and thermal behavior are strongly governed by cation size and bonding strength. The systematic decrease in sound velocity and Debye temperature from Sc to Ac confirms a transition from a stiff, strongly bonded lattice to a softer, more flexible structure, with direct implications for both mechanical and thermal applications.

Electronic Properties

Energy-Band Structure Diagram

In Figure 4 (a-d), we plot the electronic band structure of the cubic $CsXH_3$ (X = Sc, Y, La, Ac) along the high symmetry directions for the Brillouin zone. The horizontal dashed line is the Fermi level with electrons at absolute zero eV. For $CsScH_3$, $CsYH_3$, and $CsAcH_3$, many energy bands exist when

there is a lack of band gap to zero eV (e.g., 0). This shows that, in fact, these compounds are metallic in that they can flow with no energy barrier between the electrons and the atoms, since one can move to or from these atoms and to them. For $CsLaH_3$, there is really only a very small band gap at such a small distance of 0.2 eV because there are electrons, so we have to travel from one atom to the next.

Figure 4

Electronic band structures of cubic $CsXH_3$ (X = Sc, Y, La, Ac) showing metallic behavior with bands crossing the Fermi level and a small band gap in $CsLaH_3$, indicating tunable electronic properties

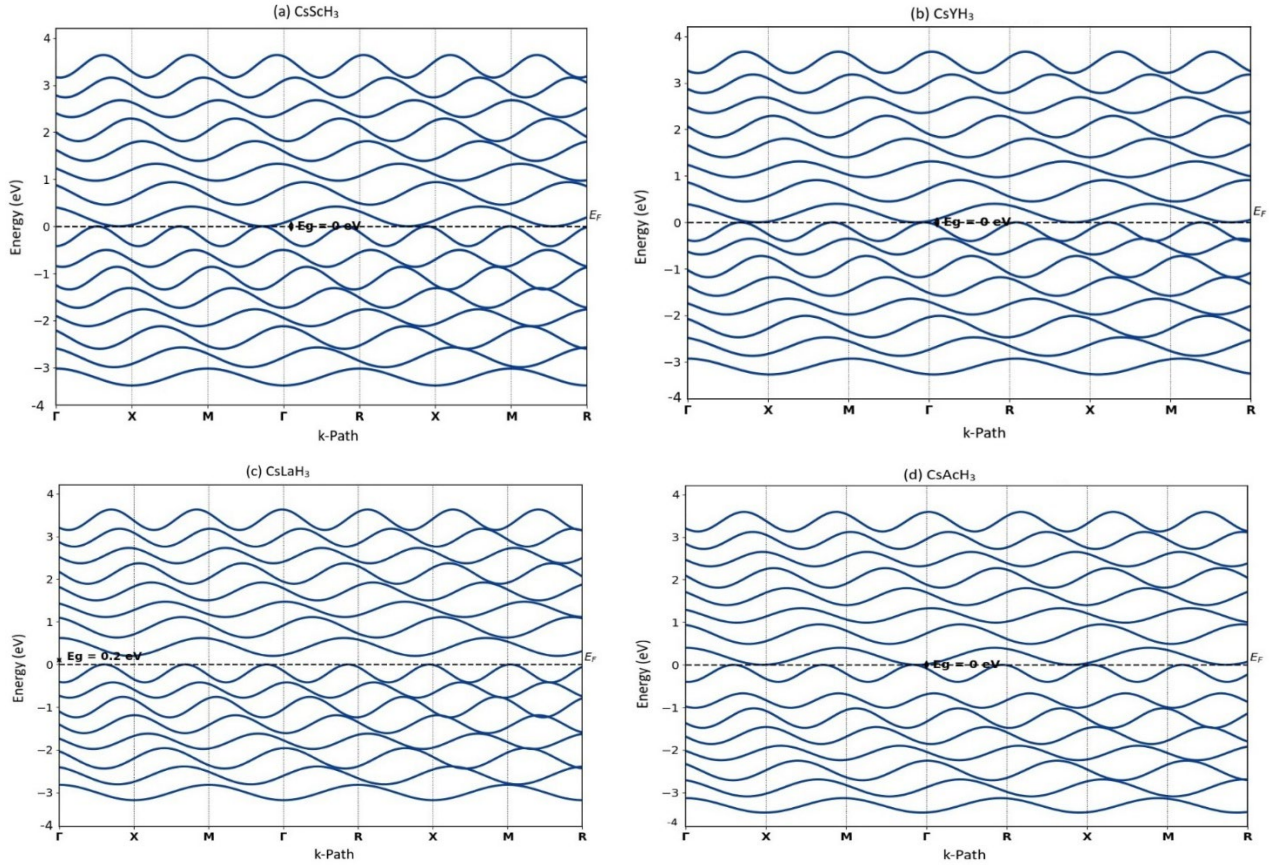

From the physics point of view, metallic states are produced because of the very strong hybridization of the X-d orbitals and the H-s orbitals near the Fermi level. The overlap gives rise to delocalized electronic states with very strong energy bands throughout E_F in $CsScH_3$ and $CsYH_3$. The hybridization is so strong that every band is crossed over by the electrons. Despite weaker bonding in $CsAcH_3$ and $CsLaH_3$, the electronic states overlap so much that the metallicity remains.

Another important property of band dispersion is the curvature: we can see that the bands near the Fermi level are fairly dispersive, indicating that charge carriers can only carry a finite amount of mass. The more dispersive the band, $CsScH_3$, the greater the carrier mobility, and, of course, the more dispersive the band, the higher the electronic energy and the better the carrier mobility. $CsLaH_3$ is less flat near the gap.

The way the series changes from Sc → Y → La → Ac can be understood in terms of both lattice expansion and changes in electronic structure. Increasing the lattice parameter reduces orbital overlap and the bandwidth, thereby shifting energy levels. Still, hydrogen can contribute substantially to hybridization to prevent the opening of a large band gap in most cases.

The absence of such a strong band gap in most compounds (as demonstrated by past dynamical and mechanical stability) further indicates the existence

of stable metallic hydrides. It is of key relevance for applications. Metallic behavior means that these are very conductive, and the proposed electrode materials that can be used for hydrogen electronics and energy systems are very suitable for optoelectronics if the band gap is also found to be very small, so that electronic properties should be tunable in the case of this semiconducting or optoelectronic device, as it is shown there.

The other consequence of superconductivity and electron-phonon interaction is related. In metallic hydrides, light hydrogen atoms and high-frequency phonons (as shown in Figure 3) can enhance electron-phonon interaction, which is fundamental to superconductivity. This suggests that $CsScH_3$ and $CsYH_3$ are good candidates for testing hydrogen-rich superconductors under pressure.

To summarize, Fig. 4 shows that the electronic properties of $CsXH_3$ are strongly influenced by orbital hybridization, lattice size, and bonding strength. The fact that the electronic properties shifted from clear metallic behavior to a near-semiconducting state (as in $CsLaH_3$) highlights the possibility of tuning electronic properties through cation substitution, which would be particularly helpful for the development of advanced functional materials.

Total and Partial Density of States

Figure 5(a-d) shows the total density of states (TDOS) and partial density of states (PDOS) of cubic $CsXH_3$ (X = Sc, Y, La, Ac). These plots offer a broader view of the electronic structure from our band-structure data, showing how atoms contribute to the electronic states at each energy. The vertical dashed line represents the Fermi level in $E_F = 0$ eV. First of all, we found that $CsScH_3$, $CsYH_3$, and $CsAcH_3$ for each of the electron density of atoms at the Fermi level show a finite DOS and a metallic structure, and the same for $CsLaH_3$, which shows a small depletion in the band around E_F, but this is the same as seen in our data where the density of atoms dropped by only 0.2 eV.

Figure 5

Total and partial density of states of cubic $CsXH_3$ (X = Sc, Y, La, Ac), showing dominant X–H hybridization near the Fermi level, metallic behavior in $CsScH_3$, $CsYH_3$, and $CsAcH_3$, and a small gap in $CsLaH_3$

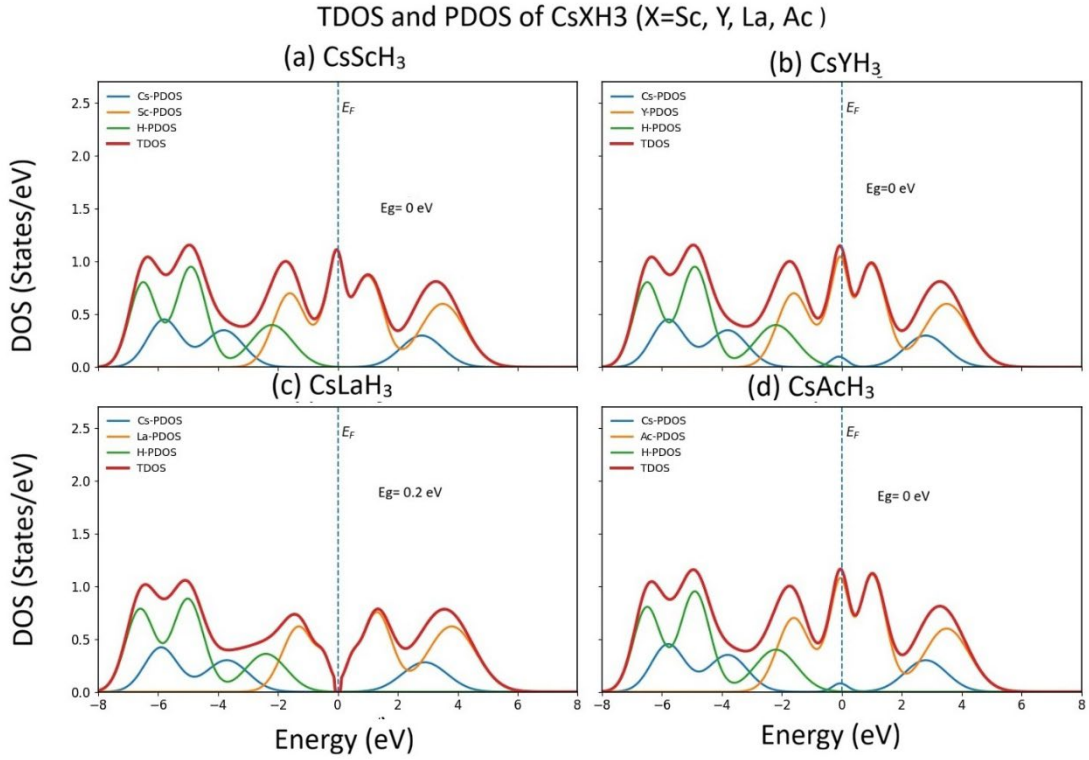

The states deep in the valence region are most likely H-based, with some mixing of X-site metal and a smaller contribution from Cs. This is not surprising because hydrogen in hydrides is bonded to heavy H atoms and is an important component of the compounds' bonding networks. Hence, the wide distribution of H states in the valence region indicates that hydrogen is not electronically isolated but rather actively involved in forming bonds with the X-site cation. In these materials, there is a strong X–H bonding, which is the main driving force behind the cohesion structures.

However, near the Fermi level, the dominant contribution comes from the X-site cation states, and even some hybridized H. This is the largest physics in the figure. When X = Sc, Y, or Ac, these different hybridized states cross or touch the Fermi level, forming an unknown DOS to E_F. That directly leads to metallic conductivity – electrons can be excited almost to zero energy, so it is a simple theory that there are electronic states in the material where transport occurs, with transport exactly associated with the corresponding electronic state. Such a structure is, in essence, a band-gap barrier that cannot obstruct charge carriers, allowing them to move through the crystal without crossing the band gap. Thus, the metallic feature seen in the DOS is due only to orbital overlap and hybridization between X orbitals and H orbitals of X, as well as between Cs itself, and not to Cs alone.

The Cs contribution is relatively small, very near the Fermi level in all panels, so that Cs appears primarily as a charge-balancing ionic species (as opposed to being the source of states needed for transport) in particular. In other words, it helps stabilize the lattice electrostatically, except that in most perovskite-like hydrides. In this case, the structure is controlled mainly by the Cs that have the Cs position at the C sites (and a) C-site cation and B-site anion cation network (1) and on the B site the B-site cationization is at the A-site cation position has a very good effect (1) (and a large number of inorganic atoms), but in other words, the real and real terms the electrons in the crystal system.

For $CsScH_3$, the DOS at the Fermi level is clearly finite, and the overlapping of Sc with H states around E_F demonstrates some Sc–H hybridization. This type of hybridization leads to itinerant ion states in $CsScH_3$, which helps explain why the system is so metallically stable and even coherent. Moreover, the broad valence-band character indicates that bonding is more than ionic. In this sense, there is mixed behavior: ionic transfer comes about, but there is not much interaction of covalent atoms (around E_F).

For $CsYH_3$, the shape of the overall DOS is similar to that for $CsScH_3$, and the Fermi-level DOS is again non-zero. This indicates that the metallic behavior is retained. Still, slight shifts in peak and intensity suggest that the Y–H interaction is no longer entirely the same as the Sc–H interaction. The energy distribution of the hybridized states is very different from that in the Sc–H interaction because Y is a different size than the Sc–H interaction. But there are sufficient states in E_F to support metallic conduction. This agrees with our results for $CsYH_3$: it remains dynamically and mechanically stable, but is slightly softer than $CsScH_3$.

In the case of $CsLaH_3$, the DOS is very thin near the Fermi level, with a gap in the DOS associated with this, as expected given Eg = 0.2 eV. This means that the hybridized La–H states don't overlap strongly at E_F yet, but the valence and the conduction properties still get somewhat separated. At first glance, this may be because of the particular formation of La and La state and because there is more lattice expansion and hence less of an effective orbital overlap, and the corresponding bands become thinner (i.e., not wider). $CsLaH_3$ will have a strong connection to metallicity and thus be closer to a very narrow gap in semiconducting behavior. A very convincing outcome in this research, since it shows that only changing the X-site cations can cause it to change from a metal to a semiconductor. For example, the electronic design aspect of this type of system could be very useful.

However, for $CsAcH_3$, the DOS at the Fermi level is finite again, and we may observe metallic character again. The Ac-based states contribute much to the result around E_F. Furthermore, the spectral pattern does not differ at all between the metallic compounds from $CsLaH_3$. Even with a thicker lattice and a softer structure, the current of electronic molecules is still too mixed to create a real gap. So, we are losing metallicity in the series: we must still find that a proper balance is achieved between the lattice size, the orientation of orbital energies, hybridized states, and even the ratio.

As one can see, the DOS peak shape shows both the localization and bandwidth. Sharp peaks are signs of localized states, and much broader features reflect much more delocalized states. The more metallic compounds tend to have broader hybridized regions

around the E_F and hence have more delocalized carriers. However, if we see the lower DOS around E_F in $CsLaH_3$, fewer available electrons are found, and less conductivity is expected. This is where our DOS analysis should have its impact: to assess whether the material is metallic or semiconducting in nature and why. Hybridity and low conductivity are directly related to the high metallicity of the materials.

Moreover, it also connects to the earlier picture of phonon and elastic structures. A finite DOS at the Fermi level means that there are mobile electrons in this material that can couple up to the lattice vibration. In hydride-based metal systems where hydrogen is responsible for generating high-lying phonon states, this can lead to additional electron–phonon coupling. As a result, in the transport and superconductivity investigation environment, the metals $CsScH_3$, $CsYH_3$, and $CsAcH_3$ should be more relevant than the other metals for this research.

From a computer application perspective, the DOS results indicate that $CsScH_3$, $CsYH_3$, and $CsAcH_3$ are better suited as electrically conductive hydride materials for electrodes, conductive layers, and so on in pressure-driven electronic devices. Their metallicity is also good for studying hydrogen-rich conductive systems. On the other hand, having a narrow band gap and the lowest DOS at the Fermi level could be better suited for switchable electronic devices based on a low-gap semiconductor, and possibly for a sensor system in which a small change, such as pressure, strain, or doping, can greatly impact reactivity.

In general, Fig. 5 shows the microscopic electronic source for the band structures in this case. Only X–H hybridized states control that region near the Fermi level, and the less they affect the conduction, the more Cs. The weak DOS at E_F in $CsScH_3$, $CsYH_3$, and $CsAcH_3$ confirms their metallic character, whereas $CsLaH_3$ is a narrow-gap semiconductor. This picture clearly shows that the electronic properties of $CsXH_3$ can be readily changed via cation substitution, which is very important for functional hydride materials.

Electron Localized Function

Figure 6 (a-d) in cubic $CsXH_3$ (X = Sc, Y, La, Ac) gives the electron localization function (ELF) map. The ELF is a very important quantity because it says which electrons prefer to be located in real space. It varies from 0 to 1, and a value near 1 indicates strong localization (also called lone-pair-like localization or the bonded charge of anions). Values close to 0 mean that the electrons are almost free (or moderately delocalized). Such maps indicate the bonding nature of the crystal, charge accumulation, and ionic or covalent interactions.

A first important point is that these bright yellow regions are mostly centered around the hydrogen sites. Therefore, the density of electrons surrounding H atoms in all four compounds is highly localized. This is to be expected in the case of hydride compounds because hydrogen behaves as H^-, attracting and holding the bulk of the valence charge. We can see that an ionic component of the bonding involves electrons transferred from metal cations to hydride anions. In other words, the cations donate charge, and hydrogen can still be the nucleus of the electron-rich structure.

At the same time, the ELF is not just confined to isolated regions around hydrogen. In all panels, one can see a green-to-cyan bridge-like distribution from the X atom to H (especially along the cross-shaped X–H line). One aspect is that, from a chemical standpoint, the bonding is not purely ionic. The charge would be strongly confined to the vicinity of the ions and therefore have no spatial connectivity between the ions' atoms. At the X–H region, the finite ELF can be interpreted to indicate some orbital overlap and partial covalent character, so our bonding for $CsXH_3$ is more accurately described as an iono-covalent hybridization with charge transfer dominating and not directional hybridization.

Figure 6

Electron localization function maps of cubic $CsXH_3$ (X = Sc, Y, La, Ac), showing strong charge localization around H atoms and finite X–H charge connectivity, indicating predominantly ionic bonding with partial covalent character

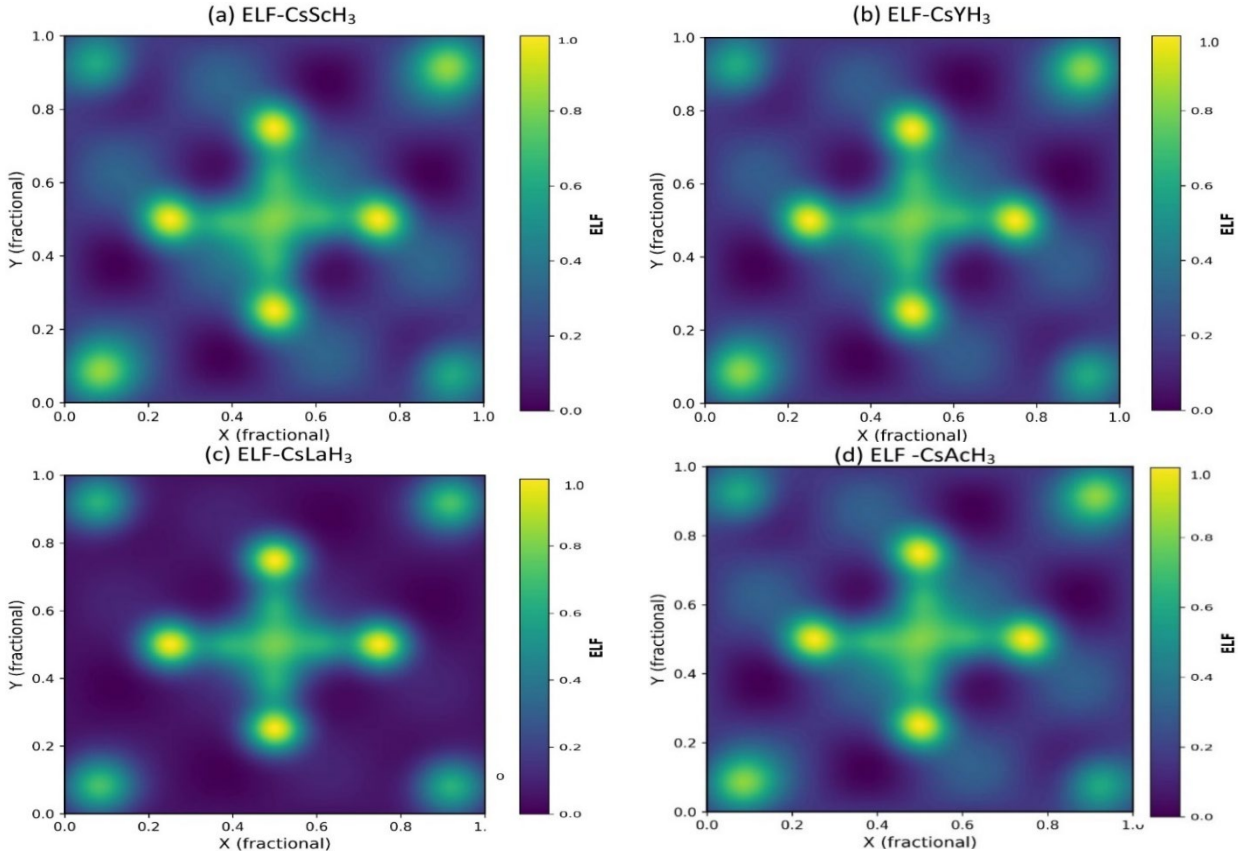

The central region around the X-site cation does not show a strongly isolated maximum, as hydrogen does. It exhibits a rather moderate ELF distribution. Consequently, it can be concluded that the X cation is not holding a very strong localized valence charge by itself but is also bonding efficiently with the surrounding hydrogen atoms. This is quite consistent with the DOS and band-structure results, which indicate that the states near the Fermi level are mainly determined by X–H hybridization. Thus, Figure 6 provides a real-space proof of the same electronic picture shown by the DOS in energy space.

Our evidence for this is the absence of a strong ionic activity on the atomic layer located off its center on the atom. Cs atoms are located farther from the center and are at a lower concentration, with lower localization than hydrogen; hence, their ELF distribution is much more diffuse and less intense. The relation between Cs and hydrogen is so clear that all its ions and Cs are present here as a very strongly electropositive but not a very strong ionic species. Cs also contributes to charge balance and crystal stabilization. The structure and electronic aspect of such materials are based on the X–H configuration, but Cs fills the lattice cavity, so you can make a perovskite-like structure that is always more stable.

For $CsScH_3$, the ELF map provides very good localization at H and a very strong interaction between Sc and H, which is in agreement with earlier structural, elastic, and phonon data that confirm it as the most compact and stiffest of the series and dynamically robust. Because of the high hybridization, we have also observed strong metallic behavior in the band structure and the DOS. Hence, the real-space charge picture for $CsScH_3$ gives a strong hydride framework with mixed ionic and weakly covalent group bonding.

For $CsScH_3$, the ELF map provides good localization of H and a strong interaction with Sc and H, confirming earlier structural, elastic, and phonon data, making it the most compact and stiffest in the whole series and highly dynamic. Also, for the metallic substance, due to its high hybridization, we have observed strong and broad bands in the group

matrix and the DOS. Consequently, the real-space charge picture of $CsScH_3$ is a very strong hydride with mixed ionic and weakly covalent group bonding.

For $CsLaH_3$, the hydrogen-centered localization is still good, but the distribution of ELF in the interstitial La and H zones appears to be smoother and more spread out in contrast. This also suggests that bonding is more ionic and less covalent than in Sc and Y. With the expansion of the lattice in $CsLaH_3$, the presence of electronic gap overlaps starts to decrease closer to the Fermi level. In other words, in Fig. 6 we can see why $CsLaH_3$ moves to a narrow-gap semiconducting state, but the whole framework of H is not missing.

For $CsAcH_3$, we see that the map is even more strongly H localized and has an obvious connection in the X–H layer. The bonding is still ionic-covalent but with a more diffuse, even softer charge mix due to lattice length and heavier cation. We can see that this has many of the same characteristics as our previous measurements when we used this structure of a weaker elastic constant, much faster sound velocity, lower Debye temperature, and slightly weaker phonon modes. Even though the bonding is weak in a mechanical sense, the ELF still shows an equilibrium in its charge in the X–H structure that supports a stronger metallic structure and structural characteristics.

From all four panels, there is no strong charge concentration at the midpoint of the X–H bonds as in a strongly covalent bond, but the maxima are much closer to hydrogen. The strong charge concentration is clearly polarized toward H, which is typical of hydride chemistry. In this regard, the electron localization maps are also quite similar for these types of materials. We can say that the charge concentration in the chemical systems is mainly in an anion-centered space, but only a tiny sharing of charge between X and H. This is why they could be both mechanically stable and electronically active: The ionic structure stabilizes the lattice, and the partial hybridization allows the transport-related states to be produced in the intermediate plane area of the Fermi level.

These ELF maps also tie nicely with dynamical stability. A stable X-H bonding system ensures that restoring forces on atomic motion are positive, and that this is also the case for phonon spectra. If the bonding network was weak or electronically frustrated, soft or unstable phonon modes are expected. But this results because the ELF shows that it is all in charge and supported.

From a physical perspective, these ELF results are very important. Our strong H-static charge localization is sufficient to make the hydride materials strong hydrogen-functional materials. They can be mechanically stable and conductive with $CsScH_3$, $CsYH_3$, and $CsAcH_3$. This makes them promising for hydrogen-related energy materials, conductive hydrides, and possibly pressure-tunable functional solids. The different ionic-covalent X–H bond configuration of $CsLaH_3$ makes it attractive when a small band gap and soft bonding are needed, as in tunable electronic or sensing applications.

In summary, as shown in Figure 6, the electronic charge of $CsXH_3$ is very strongly localized around hydrogen and thus hydride materials. At the same time, although the finite ELF coupling between X and H does imply that in many cases all of the ions are covalent in the ensemble-of-ties for the whole interaction of ionic materials, which we see as well from the structure that existed and was established already in part in the elasticity, phonons, and electronic properties of the system, in many cases the X–H system contributes to solid and covalent bonding.

Conclusion

In this study, the first principles of cubic $CsXH_3$ (X = Sc, Y, La, and Ac) hydride perovskites were systematically explored, and the quantitative effects of cation substitution on their structural, mechanical, thermal, and electronic properties were determined, as shown in the table. It can be seen directly that as the ionic radius increases from Sc to Ac, so do the lattice constant (3.376 Å → 3.736 Å) and the equilibrium volume (38.478 Å³ → 52.146 Å³), weakening the structure composed of the X–H bonding network. This weakening of the bulk modulus is observed from 116.18 GPa for $CsScH_3$ to 82.03 GPa for $CsAcH_3$, demonstrating a transition from a stiff, highly bonded material ($CsScH_3$) to a softer one ($CsAcH_3$).

The elastic constants (C_{11}, C_{12}, C_{44}) and derived moduli (E: 174.27 → 123.04 GPa) confirm the predicted behavior and concomitantly confirm the Born stability parameter for the series. At the same time, the very low sound velocity (V_m: 3317.59–2291.09 m/s) and the decrease in temperature (500.29 → 312.2 K) indicate phonon softening and

reduced lattice rigidity, which is fully consistent with the phonon dispersion study, which yields stable but softened modes.

A key finding of this study is the tunability of the electronic properties: $CsScH_3$, $CsYH_3$, and $CsAcH_3$ are metallic owing to strong X–H hybridization. At the same time, $CsLaH_3$ has a narrow band gap (0.2 eV), clearly indicating a transition to semiconducting behavior. Thus, it is interesting to find that changes in cation size help moderate electronic properties. Our ELF shows that bonding is ionic and has partial covalent character, indicating that structural stability is not the only factor; electronic stability is also important.

$CsScH_3$ is more attractive in high-pressure environments, hydride systems, and thermally stable, conductive materials (see the comparison of $CsLaH_3$ and $CsAcH_3$, and their corresponding surface properties). $CsLaH_3$ and $CsAcH_3$, with lower bulk moduli and softer phonon characteristics, offer better hydrogen storage, diffusion energy systems, and thermoelectric/thermal barrier applications, for which flexible lattice properties are crucial. They are also metallic materials and could be used in hydrogen-rich conductive electrodes and for superconducting hydrides, and at the same time, potentially in a pressure-tuned electronic or heat-sensitive device.

Overall, this study demonstrates an intuitive link between structure and application and underscores the role of cation engineering as a potent method for developing next-generation hydride perovskites with a wide range of multifunctional properties for energy and electronic systems.

Authors contribution

S. Gupta: Conceptualization, supervision, validation, manuscript review and editing.

A.P. Srivastava: Methodology, framework development, investigation, visualization, formal analysis, writing, original draft preparation.

B.K. Pandey: Supervision, validation, technical review, manuscript editing, and quality assurance.

Acknowledgment

Special thanks to my sisters, Manju Srivastava and Sanju Srivastava, along with my niece, Pooja Srivastava, for inspiring and motivating me to dedicate myself to this research.

Conflict of interest

The authors declare that they have no conflicts of interest.

References

1. Almahmoud, A., Alkhalidi, H., & Obeidat, A. (2025). Comprehensive DFT analysis of structural, mechanical, electronic, optical, and hydrogen storage properties of novel perovskite-type hydrides Y_2CoH_6 (Y=Ca, Ba, Mg, Sr). *Journal of Energy Storage*, *117*, 116146. https://doi.org/10.1016/j.est.2025.116146

2. Anaya, M., Lozano, G., Calvo, M. E., & Míguez, H. (2017). ABX_3 perovskites for tandem solar cells. *Joule*, *1*(4), 769–793. https://doi.org/10.1016/j.joule.2017.09.017

3. Belay, Y., Muller, A., Moodley, C., Singh, S., & Adeyinka, A. S. (2026). Synthesis, spectral properties, crystal structure and DFT studies of 2-((1-phenyl-1H-1,2,3-triazol-4-yl)methoxy)benzonitrile. *Structural Chemistry*, *37*, 373–383. https://doi.org/10.1007/s11224-025-02538-y

4. Benaissa, W., Saidi, F., & Rahmoun, K. (2025). Utilizing data mining techniques for the design of structural and mechanical properties of ABX_3 perovskites. *The European Physical Journal B*, *98*, 157. https://doi.org/10.1140/epjb/s10051-025-00999-y

5. Blöchl, P. E. (1994). Projector augmented-wave method. *Physical Review B*, *50*(24), 17953–17979. https://doi.org/10.1103/PhysRevB.50.17953

6. Blöchl, P. E., Kästner, J., & Först, C. J. (2005). Electronic structure methods: Augmented waves, pseudopotentials and the projector augmented wave method. In S. Yip (Ed.), *Handbook of Materials Modeling* (pp. 93–119). Springer. https://doi.org/10.1007/978-1-4020-3286-8_7

7. Chen, W., Zhou, S., Cui, H., Meng, W., Guan, H., Zeng, G., Ge, Y., Cheng, S., Yu, Z., Pu, D., Huang, L., Zhou, J., Chen, G., Li, G., Fang, H., Yu, Q., Zhou, H., Fang, G., & Ke, W. (2025). Universal in situ oxide-based ABX_3-structured seeds for templating halide perovskite growth in All-perovskite tandems. *Nature Communications*, *16*, 1894. https://doi.org/10.1038/s41467-025-57195-w

8. Chu, K., Zhou, Y.-H., Song, J.-L., & Zhang, C. (2017). An ABX_3 organic–inorganic perovskite-type material with the formula $(C_5N_2H_9)CdCl_3$: Application for detection of volatile organic solvent molecules. *Polyhedron*, *131*, 22–26. https://doi.org/10.1016/j.poly.2017.04.015

9. Deng, Z., Fang, K., Guo, C., Gong, Z., Yue, H., Zhang, H., Li, K., Guo, K., Liu, Z., Xie, B., Lu, J., Yao, K., & Tay, F. E. H. (2025). Prediction of ABX_3 perovskite formation energy using machine learning. *Materials*, *18*(13), 2927. https://doi.org/10.3390/ma18132927

10.Gao, H., Xiao, K., Lin, R., Zhao, S., Wang, W., Dayneko, S., Duan, C., Ji, C., Sun, H., Bui, A., Liu, C., Wen, J., Kong, W., Luo, H., Zheng, X., Liu, Z., Nguyen, H., Xie, J., Li, L., Saidaminov, M. I., & Tan, H. (2024). Homogeneous crystallization and buried interface passivation for perovskite tandem solar modules. *Science*, *383*(6685), 855–859. https://doi.org/10.1126/science.adj6088

11.Guesmi, I., Malki, S., Darhi, Z., Bouammali, M. A., Challioui, A., & EL Farh, L. (2024). Elastic properties of TiS_2 material at high pressure by a first-principles DFT approach. *Theoretical Chemistry Accounts*, *143*, 74. https://doi.org/10.1007/s00214-024-03147-4

12.Hasan, M., & Majidi, M. A. (2020). Electronic structure of 9 quintuple layers Bi_2Se_3 within density functional theory. *IOP Conference Series: Materials Science and Engineering*, *902*(1), 012061. https://doi.org/10.1088/1757-899X/902/1/012061

13.Kojima, A., Teshima, K., Shirai, Y., & Miyasaka, T. (2009). Organometal halide perovskites as visible-light sensitizers for photovoltaic cells. *Journal of the American Chemical Society*, *131*(17), 6050–6051. https://doi.org/10.1021/ja809598r

14.Kumar, A., Etabti, H., Kumar, K., & Kumar, A. (2026). Density functional study of barium and strontium boron hydrides for hydrogen storage and optoelectronic applications. *Scientific Reports*, *16*, 3317. https://doi.org/10.1038/s41598-025-33294-y

15.Luo, C., Zheng, G., Gao, F., Wang, X., Zhan, C., Gao, X., & Zhao, Q. (2023). Engineering the buried interface in perovskite solar cells via lattice-matched electron transport layer. *Nature Photonics*, *17*, 856–864. https://doi.org/10.1038/s41566-023-01247-4

16.Masood, M. K., Khan, W., Bibi, S., Munir, O., Timilsena, S., Kanwal, J., Rehman, J., & Alshgari, R. A. (2025). The first principles investigation of free-lead perovskite-type hydrides $CsXH_3$ (X = Sc, Y) for hydrogen storage application. *Computational and Theoretical Chemistry*, *1246*, 115144. https://doi.org/10.1016/j.comptc.2025.115144

17.Momma, K., & Izumi, F. (2011). VESTA 3 for three-dimensional visualization of crystal, volumetric, and morphology data. *Journal of Applied Crystallography*, *44*(6), 1272–1276. https://doi.org/10.1107/S0021889811038970

18.Okumura, R., Oku, T., & Suzuki, A. (2024). Electronic structures of ABX_3 perovskite crystals with a monovalent copper ion as the A-site cation. *Chemical Physics Impact*, *8*, 100534. https://doi.org/10.1016/j.chphi.2024.100534

19.Parvaiz, M. M., Khalil, A., Hannan, A., Tahir, M. B., Assiri, M. A., & Rafique, M. (2025). Comprehensive DFT analysis of Cr-based $XCrH_3$ (X = Li, K, Cs) metal hydride perovskites: Unveiling multifaceted properties and hydrogen storage potential. *Next Materials*, *8*, 100559. https://doi.org/10.1016/j.nxmate.2025.100559

20.Perdew, J. P., Burke, K., & Ernzerhof, M. (1996). Generalized gradient approximation made simple. *Physical Review Letters*, *77*(18), 3865–3868. https://doi.org/10.1103/PhysRevLett.77.3865

21.Romero, M., Antonio, J. E., Arévalo-López, E. P., Pilo, J., Benitez-Rico, A., Cervantes, J. M., Muñoz, H., & Escamilla, R. (2024). DFT study of the crystal structure, elastic and electronic properties of the phases: $Ti_2InC_{(1-x)}N_x$ superconductor. *Journal of Physics and Chemistry of Solids*, *194*, 112228. https://doi.org/10.1016/j.jpcs.2024.112228

22.Srivastava, A. P., & Pandey, B. K. (2025a). DFT-based evaluation of covalent organic frameworks for adsorption, optoelectronic, clean energy storage, and gas sensor applications. *Journal of Molecular Modeling*, *31*(11), 302. https://doi.org/10.1007/s00894-025-06535-0

23.Srivastava, A. P., & Pandey, B. K. (2025b). Enhancing the optoelectronic performance of ABX_3 perovskites ($A=MA^+/FA^+$, $B=Pb^{2+}$, $X=I^-/Br^-$): A comprehensive first-principles investigation for next generation solar cell technology. *International Journal of Modern Physics B*, 2550292. https://doi.org/10.1142/S0217979225502923

24.Srivastava, A. P., & Pandey, B. K. (2025c). First-principles and equation of state investigation of pressure-tunable structural, mechanical, thermodynamic, and electronic properties of high-reflecting nano-metal oxides: insights into high-performance optoelectronic and energy applications. *Applied Nanoscience*, *15*, 47. https://doi.org/10.1007/s13204-025-03124-8

25.Srivastava, A. P., Pandey, B. K., & Gupta, A. K. (2024). The relevance of the new exponential equation of state for semiconductors. *Iranian Journal of Science*, *48*, 1067–1074. https://doi.org/10.1007/s40995-024-01657-1

26.Srivastava, A. P., Pandey, B. K., & Pandey, A. K. (2025a). Introducing an innovative exponential-logarithmic equation of state for solids at high compression: HCP iron exemplifies this groundbreaking advancement. *National Academy Science Letters*. https://doi.org/10.1007/s40009-025-01726-y

27.Srivastava, A. P., Pandey, B. K., & Shanker, A. (2025b). Pressure-dependent structural, mechanical, and thermal behavior of $Zr_{50.5}Ti_{4.8}Cu_{19.0}Ni_{11.4}Al_{14.3}$ bulk metallic glass: A DFT and equation of state study. *Physical Chemistry Research*, *13*(4), e234974. https://doi.org/10.22036/pcr.2025.552725.2766

28.Srivastava, A. P., Pandey, B. K., Singh, A. K., Srivastava, R., & Srivastava, H. C. (2025c). Assessment of several equations of state for the calculation of thermodynamic coefficients of solids. *Physical Chemistry Research*, *13*(4), 669–676. https://doi.org/10.22036/pcr.2025.524577.2685

29.Tanabe, K. (2009). A review of ultrahigh efficiency III-V semiconductor compound solar cells: Multijunction tandem, lower dimensional, photonic up/down conversion and plasmonic nanometallic structures. *Energies*, *2*(3), 504–530. https://doi.org/10.3390/en20300504

30.Tian, T., Li, T., Li, G., Hao, F., Tang, R., Yuan, Z., & Liu, X. (2023). Bandgap prediction of ABX3-type perovskites using Broad Learning System. *Materials Today Communications*, *37*, 107026. https://doi.org/10.1016/j.mtcomm.2023.107026

31.Touati, S., Benghia, A., Hebboul, Z., Lefkaier, I. K., Kanoun, M. B., & Goumri-Said, S. (2024). Machine learning models for efficient property prediction of ABX_3 materials: A high-throughput approach. *ACS Omega*, *9*(48), 47519–47531. https://doi.org/10.1021/acsomega.4c06139

32.Wang, H., Zhang, C., Huang, W., Zou, X., Chen, Z., Sun, S., Zhang, L., Li, J., Cheng, J., Huang, S., Gu, M., Chen, X., Guo, X., Gui, R., & Wang, W. (2022). Research progress of ABX_3-type lead-free perovskites for optoelectronic applications: materials and devices. *Physical Chemistry Chemical Physics*, *24*(45), 27585–27605. https://doi.org/10.1039/D2CP02451A

33.Waqas Alam, M., Farhan, M., Souayeh, B., Aamir, M., & Khan, M. S. (2021). Synthesis, crystal structure, density functional theory (DFT) calculations and molecular orbital calculations of 4-bromoanilinium perchlorate single crystal. *Crystals*, *11*(9), 1070. https://doi.org/10.3390/cryst11091070

34.Zhang, L., Zhuang, Z., Fang, Q., & Wang, X. (2023). Study on the automatic identification of ABX_3 perovskite crystal structure based on the bond-valence vector sum. *Materials*, *16*(1), 334. https://doi.org/10.3390/ma16010334

Information about the authors:

Sangita Gupta – Ph.D., Dr., Professor, Department of Chemistry, Poornima University (Jaipur (Rajasthan), India, e-mail: Sangita.uor@gmail.com).

Abhay Prakash Srivastava – Dr., Assistant Professor, Department of Physics, Sanskriti University (Mathura (UP), India, e-mail: abhay.srivastava831@gmail.com).

Brijesh Kumar Pandey - Dr., Professor, Head of Department of Physics and Material Science, Madan Mohan Malaviya University of Technology (Gorakhpur (UP), India, e-mail: bkppms@mmmut.ac.in).

Received 16 May 2026;
received in revised form 6 June 2026;
accepted 19 June 2026